Optical Engineering

OpticalEngineering.SPIEDigitalLibrary.org

Laser scanner module with large sending aperture and inherent high angular position accuracy for three-dimensional light detecting and ranging

Jürgen Hasselbach
Siegwart Bogatscher
Christian Rembe

SPIE.

Jürgen Hasselbach, Siegwart Bogatscher, Christian Rembe, "Laser scanner module with large sending aperture and inherent high angular position accuracy for three-dimensional light detecting and ranging," *Opt. Eng.* **58**(8), 087101 (2019), doi: 10.1117/1.OE.58.8.087101.

Laser scanner module with large sending aperture and inherent high angular position accuracy for three-dimensional light detecting and ranging

Jürgen Hasselbach,[a,b,*] Siegwart Bogatscher,[b] and Christian Rembe[a]
[a]Clausthal University of Technology, Institute of Electrical Information Technology, Clausthal-Zellerfeld, Germany
[b]Robert Bosch GmbH, Chassis Systems Control, Schwieberdingen, Germany

Abstract. One design of the state-of-the-art laser scanner systems in automotive applications is based on oscillating mirror modules. The requirement of a large mirror surface for eye-safe transmission beams and long measurement distances is a major drawback for fast and reproducible scanning. Tolerances of angular positioning, position sensing, and vibrational perturbations limit the position accuracy of such a mirror and, thus, the accuracy of the transmission spot position in the field of view (FoV). Our approach for a scanner module with maximum transmission beam diameter combines a microlens array with an objective lens for generating one optical telescope assembly for each angular scan position exclusively. Aperture stops define the beam positions in the FoV and avoid positioning errors caused by angle deviations of the scanner mirror. This increases the reliability of the angular position accuracy of the scanner module significantly. To minimize the shadings between adjacent scan spots in the target distance, created by beam cutoffs at the aperture stop of the objective lens, an array of optimized microwedge prisms is provided in combination with the microlens array. Therefore, we can increase the throughput of transmission power into the FoV and improve the measurement distance, especially at large scan angles. [DOI: 10.1117/1.OE.58.8.087101]

Keywords: laser scanner; microelectromechanical system/micro-optoelectromechanical system scanner; three-dimensional light detecting and ranging; large aperture; eye-safe laser scanner; angular accuracy.

Paper 190346 received Mar. 11, 2019; accepted for publication Jul. 2, 2019; published online Aug. 7, 2019.

1 Introduction

Typically, there are two system principles of time-of-flight distance measurement, namely, scanner systems and three-dimensional camera/flash light detecting and ranging (LiDAR) systems. While scanner systems illuminate and collect each object point in the field of view (FoV) sequentially,[1,2] flash LiDAR systems measure the entire FoV simultaneously in one snapshot.[3,4] Hence, high frame rates are realized without smearing effects of moving objects. Owing to a solid-state setup, each measurement point relates to a fixed field angle and can be detected by one certain receiver element. This allows a precise spatial assignment of object points in the FoV, which leads to a high absolute angular accuracy of the system. The maximum measurable range of flash LiDAR systems is smaller with respect to scanner modules if the FoV size and transmission power per pulse are identical. The advantage of scanner modules regarding measurement ranges results from a higher level of receiving signal due to the concentration of the laser power to one measurement point, while flash LiDAR requires simultaneous illumination of the entire FoV. In terms of realizing the specifications of obstacle recognition and FoV surveillance in automotive applications, typically, scanner systems are the preferred technology in the market.[5,6] Concerning transmission power consumption, the trade-off between meaningful measurement distances (<100 m)[6,7] and horizontal FoV dimensions (>±20 deg)[8] is obligatory for flash LiDAR systems. The power consumption exceeds by factors compared to that of scanner systems, which is why the common operating range of flash systems is around 0.1 to 25 m.[3,7]

The state-of-the-art laser scanner systems in automotive applications are based on transmission signal deflection modules with large, heavy and expensive oscillating or rotating mirrors. For transmitting eye-safe laser beams and collecting maximum amounts of scattered and reflected signal of measured targets in the FoV, large sending and receiving apertures, which means large scanning mirror surfaces, are essential. The reachable distance up to 200 m and the corresponding distance uncertainty is typically in the range of 2 mm to 10 cm, depending on the environmental conditions and ambient illumination. The range of angular resolution is around 0.01 deg to 0.5 deg with an angular uncertainty up to 0.015 deg.[5–9] However, the large construction size, the fine mechanics setup, as well as low potential of automated high volume manufacturing seem to be the major drawbacks of this kind of scanner design.

Replacing the fine-mechanical deflection mirror by a microelectromechanical system (MEMS) scanning mirror overcomes the large construction size. However, a smaller scanning mirror size reduces the sensor aperture and, therefore, the measurement distance. Consequently, a mirror array or a very large single MEMS mirror setup is in the range of typically 1- to 11-mm diameter.[9–12] On the one hand, the cost factor rises directly with the active mirror area.[13] On the other hand, the requirement of a large MEMS mirror surface is a major drawback for fast and reproducible scanning. Tolerances of angular positioning, position sensing, as well as vibrational perturbations, e.g., externally induced shock lead to mirror-deflection noise, which is projected directly into the FoV. Thus, the resulting position noise of measurement

*Address all correspondence to Jürgen Hasselbach, E-mail: juergen.hasselbach@de.bosch.com

spots in the FoV is the main reason for the limitation of the accuracy of spot positions.

Add-on closed-loop feedback circuits realize the measurement of the actual mirror position. The position can be readout either optically on the basis of the position of reflected signal on a monitor diode at the backside of the mirror[14] or piezoelectrically through the measurement of torsion at the mirror springs while oscillating.[15] However, with this technique several vibration modes can cause ambiguous position feedback. A further possibility is to measure the capacity variation depending on the overlapping depth of finger structures at the mirror.[16,17] The reachable angular uncertainty in closed-loop circuit modules is located in the range around 0.015 deg to 0.1 deg.

By increasing the mirror surface, the inherent dynamic deformation $\delta_{\mu M}$ increases with the mirror diameter $d_{\mu M}$ ($\delta_{\mu M} \propto d_{\mu M}^5$) while oscillating, especially in the turning points. In addition, the static deformation induced by tensions between particular mirror layers becomes more relevant.[18,19] To scale-up the mirror thickness $t_{\mu M}$ ($\delta_{\mu M} \propto 1/t_{\mu M}^2$) is one possibility of reducing the deformations $\delta_{\mu M}$. This again leads to higher mass of the mirror $m_{\mu M}$ and, respectively, higher inertia $I_{\mu M}$ ($I_{\mu M} \propto d_{\mu M}^2$, assumed a round mirror surface). Higher inertia and higher rotating angles $\varphi_{\mu M}$ correspond to increasing torsional stress κ_S in the mirror springs ($\kappa_S \propto I_{\mu M} \propto \varphi_{\mu M}$). For fast retraction, a higher stiffness of springs is advantageous, which increases the stress level and the postoscillation. Complementarily, this reduces the shock and vibration resistivity.[19–21] In conclusion, regarding lifetime and robustness aspects, the target for the operation of a scanning mirror module is minimum dimensions $d_{\mu M}$ and low deflection angles $\varphi_{\mu M}$.

As presented in Refs. 22 and 23, scanner systems, including micro-optics, are an alternative approach for maximization of the sending and receiving apertures without increasing the mirror surface. Here, the assembly of one micro-optical element with an objective lens generates an optical telescope for each separate scan position exclusively.[24–26] The maximum transmission beam diameter and the maximum receiving aperture of these systems accordingly depend on the combination of microlens and objective lens. Transmission beam cutoffs at the aperture stop of the objective lens turn out to be an inherent system drawback while scanning over a microlens array. The consequence is a significant loss of measurement distance and an intermittently sampled FoV at large field angles.

In this paper, we present the approach for a scanner module based on prior work.[22,23] This scanner module improves the position accuracy of measurement spots in the FoV without any shadings in between. Among others, we show in detailed simulation and measurement the influence of spot position noise and beam cutoffs on the transmission power. Usually, mirror-deflection noise is the dominant limitation for the position accuracy of the measurement spots. We design the dimensions of aperture stops between the microlenses and the transmission beam diameter on the microlens array carefully in order to suppress the direct projection of the angular noise of the rotating mirror into the FoV. Therefore, our new design approach leads to a system with inherent high measurement spot-position accuracy. In addition, the design of a specific microwedge prism for each particular microlens avoids previously described transmission beam cutoffs at the aperture stop of the objective lens. This avoids resulting shadings between adjacent scan spots in the FoV and increases the throughput of transmission power into the FoV. The consequence is the improvement of measurement distance, especially at large scan angles.

2 Laser Scanner Module

The geometrical correlations of the actual scanning principle are described in Sec. 2. We also show the system limitations regarding reachable transmission beam diameters and the correlated maximum allowed transmission power. This consideration is in conformity to the IEC 60825-1:2014 standard.

2.1 *Principle of the Laser Scanner Module*

In this paper, we present a laser scanner system (Fig. 1), which realizes large transmission beam diameters with minimum mirror dimensions and rotation angles. We derive an equation for the two-dimensional (2-D) rotating angles $\varphi_{\mu M}$ of the oscillating mirror μM to hit the center position of each microlens on the microlens array MLA_T with the deflected transmission beam optimally [see Fig. 2(a)]. The necessary angle depends on the incoming transmitter vector $\vec{V}_{T_{in}}$ on mirror μM, the inclination angle β_{MT} of mirror MT, and the center positions of the microlenses on the microlens array MLA_T. For better clarity, Figs. 1(a) and 2 just show the yz-plane. The rotation angle of the mirror μM around the y-axis with $\varphi_{\mu M,y}$ in the xy-plane is derived analog to the rotation angle around the x-axis with $\varphi_{\mu M,x}$ in the yz-plane. We also show the derivation of the divergence angle θ_T in dependence on the focal length $f_{\mu L}$ and the diameter $d_{\mu L}$ of the microlens. It also depends on the distance $a_{\mu L}$ of the microlens to the objective lens (Lens LO) and its focal length f_{LO}.

The scanner module provides the classification of laser class 1 in conformity with the IEC 60825-1:2014 standard. Our system incorporates an optimized micro-optical array for noise suppression of the transmitted spot position in the FoV. The optics solution additionally avoids shadings in the FoV for high light-collecting efficiency even at large field angles. These characteristics allow high robustness against vibrational perturbations and front lens contaminations, as well as constant angular resolution within maximum measurement range. The separation of optical paths in the setup gives a high stray light insensitivity of transmission signal reflections at components in the transmitter path. In addition, the setup allows separate optical design of the microlens arrays for particular transmission and receiving requirements.

Figure 1(a) shows the optical operating principle of the scanner module and, respectively, the equivalent demonstrator setup [see Fig. 1(b)]. Outgoing from the laser source (transmitter), the transmission beam (T_0 and T_n for one exemplarily angular mirror position each) is deflected via a MEMS mirror μM to the lens LT, which converts the rotational movement of mirror μM to a parallel shift to the optical axis. This again realizes a sampling of each microlens perpendicular to its principal plane on the microlens array MLA_T. Depending on the focal length f_{LT} of lens LT, the necessary rotation angle of mirror μM correlates directly to the resulting parallel shift of T_0 to T_n. The beam-shaping

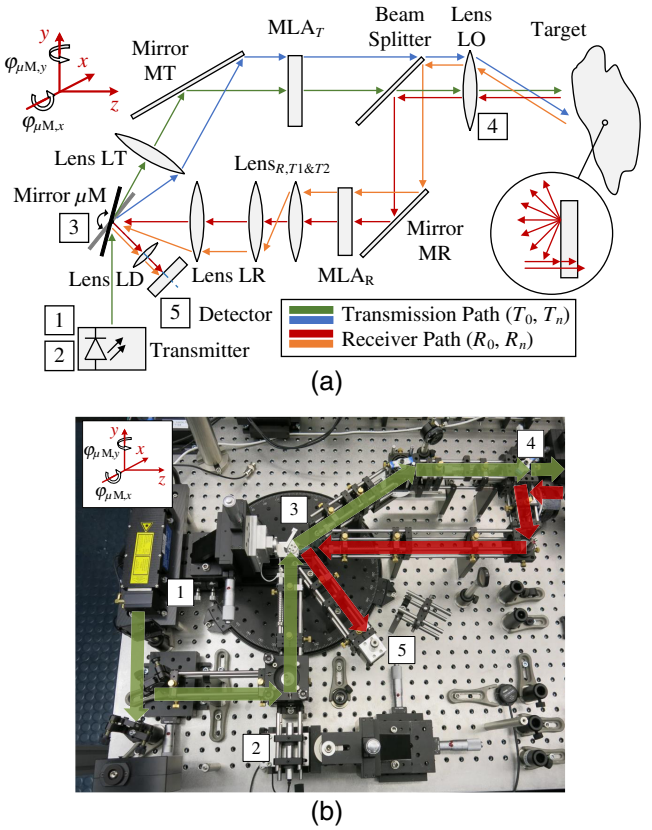

Fig. 1 Setup of the laser scanner module. For better clarity, just the yz-plane is shown here. (a) Schematic depiction of the optical path inside the scanner module, with the help of two sequentially transmitted laser beams (T_0 and T_n for one mirror position each) and the corresponding received signal on the detector after scattering at the target (R_0 and R_n). (b) Demonstrator setup with (1) Crylas FDSS 532-Q laser, (2) Thorlabs CPS532-C2 alignment laser, (3) Smaract STT-2013 2-D motorized optical mount, (4) Olympus M. Zuiko Digital ED 25 mm F1.2 Pro standard objective lens, and (5) IDS UI-1450-C USB 2.0 camera (for testing issues).

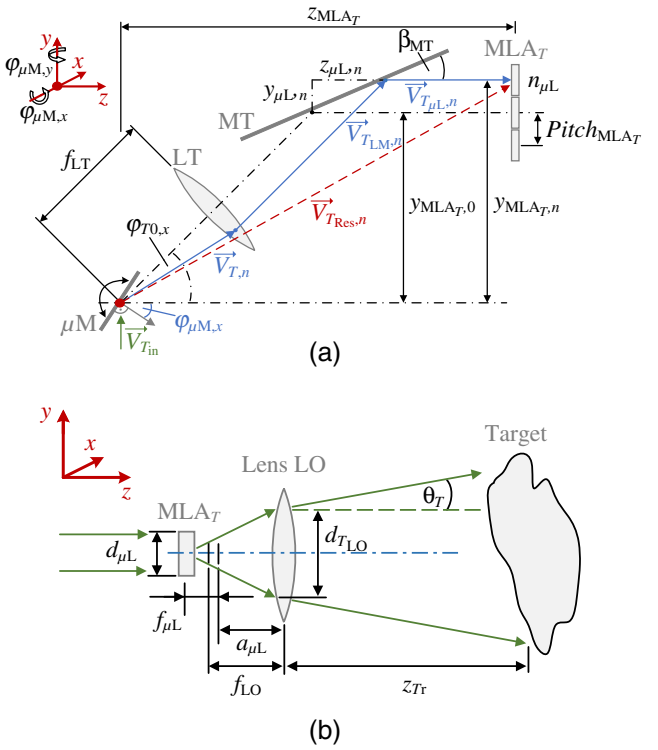

Fig. 2 Geometrical operation principle of the laser scanner module. For better clarity, just the yz-plane is shown here. (a) Scanner section with the geometrical correlation of the rotational angle $\varphi_{\mu M,x}$ of the rotating mirror μM depending on the transmission vector $V_{T_{Res},n}$. This position vector describes the vector from the rotating position of mirror μM to the center position of each particular microlens on the microlens array MLA$_T$. (b) Simplified beam-shaping section with correlation between the divergence angle θ_T and the z-positioning $a_{\mu L}$ of the microlens array MLA$_T$ to the objective lens LO.

section, consisting of one microlens and the objective lens LO, generates an optical telescope assembly for each scan position and, respectively, spot position in the FoV. Therefore, the amount of microlenses on the microlens array MLA$_T$ is equal to the amount of spot positions in the FoV, assuming no subsampling on the detector. Concerning eye-safety requirements, each microlens widens the transmission beam to the size of a less critical diameter $d_{T_{LO}}$ at the system exit plane of the objective lens LO [see Fig. 2(b)]. Despite a beam widening, the advantage compared to a conventional telescope setup is no loss of field angle in the FoV at all. After scattering at the target, the receiving signal (R_0 and R_n) reaches a separate receiver path via the objective lens LO and the beam splitter. Each angular mirror position of the mirror μM corresponds to one particular incidence angle of the receiving signal (see R_0 and R_n). Accordingly, the deflection of the receiving signal can be compensated to one static position on the detector with the advantage of minimum necessary detector dimensions. Such a system setup is favorable for the design of a microlens array MLA$_T$ in the transmission path with additional aperture stops between each microlens. This design suppresses spot position noise in the FoV caused by the limited angular accuracy of the mirror μM. However, the microlens array MLA$_R$ in the receiving path can be designed with an optimized diameter of each microlens without additional aperture stops for maximum light-collecting efficiency.

The relation of the necessary 2-D rotation angles $\varphi_{\mu M,x}$ and $\varphi_{\mu M,y}$ for deflecting the transmission beam depending on the corresponding center position of each sampled microlens is illustrated in Fig. 2(a). For the following calculation, the rotation point of the rotating mirror μM is defined as the point of origin of the coordinate system (marked with the red point).

The vector $\vec{V}_{T_{Res},n}$ describes the position vector from the rotating point of mirror μM to the center position of each single microlens. In consequence, this vector is defined with the given coordinates of the microlens array MLA$_T$ ($x_{MLA_T,0}$, $y_{MLA_T,0}$, and z_{MLA_T}) as well as the pitch between each microlens $Pitch_{MLA_T}$ and the number $n_{\mu L}$ of each particular microlens in x- and y-directions

$$\vec{V}_{T_{Res},n} = \begin{pmatrix} n_{\mu L,x} \cdot Pitch_{MLA_T,x} + x_{MLA_T,0} \\ n_{\mu L,y} \cdot Pitch_{MLA_T,y} + y_{MLA_T,0} \\ z_{MLA_T} \end{pmatrix}. \quad (1)$$

The vector $\vec{V}_{T,n}$ with $\vec{V}_{T,n} = \vec{V}_{T_{Res},n} - \vec{V}_{T_{LM},n} - \vec{V}_{T_{\mu L},n}$ describes the transmission beam from the rotating point of mirror μM to lens LT to hit finally the center position of each microlens. The vector $\vec{V}_{T_{LM},n}$ describes the transmission

beam after refraction on lens LT and $\vec{V}_{T_{\mu L},n}$ is the vector after deflection at the mirror MT. The inclination angle β_{MT} of mirror MT, the angle of lens LT $\varphi_{T0,x} = 2 \cdot \beta_{MT}$, and its focal length f_{LT} are given by the system design as well. Hence, $\vec{V}_{T,n}$ can be expressed in dependence on these known system design parameters as

$$\vec{V}_{T,n} = \begin{bmatrix} x_{\mu L,n} \\ \sin(\varphi_{T0,x}) \cdot (f_{LT} - C_1) \cdot \sin\left(\frac{\varphi_{T0,x}}{2}\right) \cdot \frac{1}{\tan(\varphi_{T0,x})} \\ \cos(\varphi_{T0,x}) \cdot (f_{LT} + C_1) \cdot \sin\left(\frac{\varphi_{T0,x}}{2}\right) \cdot \tan(\varphi_{T0,x}) \end{bmatrix}, \tag{2}$$

where $x_{\mu L,n} = n_{\mu L,x} \cdot \text{Pitch}_{MLA_T,x}$, $y_{\mu L,n} = n_{\mu L,y} \cdot \text{Pitch}_{MLA_T,y}$, $z_{\mu L,n} = \frac{y_{\mu L,n}}{\tan(\beta_{MT})}$, $C_1 = \sqrt{z_{\mu L,n}^2 + y_{\mu L,n}^2}$, and $z_{\mu L,n} = \frac{y_{\mu L,n}}{\tan(\beta_{MT})}$.

Now, we can determine the necessary rotation angle $\varphi_{\mu M}$ of mirror μM to deflect the known incoming transmitter vector $\vec{V}_{T_{in}}$ to the vector $\vec{V}_{T,n}$. In a first step we have to calculate the normalized normal vector to the mirror surface μM $\vec{V}_{u,N} = -\vec{V}_{u,T_{in}} + \vec{V}_{u,T,n}$, where $\vec{V}_{u,T_{in}}$ is the given normalized vector of the laser source and $\vec{V}_{u,T,n}$ is the known normalized vector of the transmission beam after deflection on mirror μM. Then, we calculate $\vec{V}_{Rot}$ with the inverse direction cosine matrix $\vec{V}_{Rot} = DCM_y^{-1} \cdot \vec{V}_{u,N}$, which describes the rotated vector $\vec{V}_{u,N}$ to the optical axis in z-direction. The 2-D rotation $\vec{\varphi}_{\mu M}$ to deflect the transmission beam to the center position of each microlens finally can be described as

$$\vec{\varphi}_{\mu M} = \begin{pmatrix} \varphi_{\mu M,x} \\ \varphi_{\mu M,y} \end{pmatrix} = \begin{bmatrix} \tan^{-1}\left(\frac{V_{Rot,y}}{V_{Rot,z}}\right) \\ \tan^{-1}\left(\frac{V_{u,N,x}}{V_{u,N,z}}\right) \end{bmatrix}. \tag{3}$$

In Fig. 2(b), the beam-shaping section of the scanner module is depicted in simplified form with just one microlens. It shows the correlation of the distance $a_{\mu L}$ in z-direction between one microlens and the objective lens LO. The resulting divergence angle θ_T, with help of the paraxial approximation, is expressed as

$$\theta_T = \tan^{-1}\left[\frac{\frac{d_{\mu L}}{2 \cdot f_{\mu L}} - \frac{a_{\mu L} \cdot d_{\mu L}}{2 \cdot f_{LO} \cdot f_{\mu L}}}{1 + \left(\frac{d_{\mu L}}{2 \cdot f_{\mu L}}\right)^2 \cdot \frac{a_{\mu L}}{f_{LO}}}\right], \tag{4}$$

where $d_{\mu L}$ and $f_{\mu L}$ are the diameter and the focal length of one microlens, respectively. The parameter f_{LO} describes the focal length of the objective lens LO. Hence, the divergence angle can be adjusted by varying the distance $a_{\mu L}$ between the microlens array MLA_T, and the objective lens LO. In principle, correct adjustment of θ_T offers the capability to sample the FoV without any gaps between adjacent scan spots in the FoV.

2.2 *Limitations of the Transmission Beam Diameter and Transmission Power*

The geometrical correlation between reachable FoV dimensions and angular resolution α_{Tr}, coupled with large transmission beam diameter $d_{T_{LO}}$, is one fundamental limitation of scanner systems including micro-optics for transmission beam widening. The theoretically feasible transmission beam diameter on the principal plane of the objective lens LO is limited by its diameter d_{LO}. We assume planoconvex spherical lenses with a refraction index n_{MLA_T} of 1.5 and a maximum radius of curvature $R_{\mu L}$ of half the diameter $d_{\mu L}$ of one microlens on the microlens array MLA_T. In consequence the lower limitation of focal length of one microlens is $f_{\mu L,min} = 2 \cdot R_{\mu L}$, which results in a f-number $F\#_{\mu L} = f_{\mu L}/d_{\mu L} \geq 1$.[27] Here, a microlens with $F\#_{\mu L} = 1$ defines the minimum possible focal length $f_{\mu L,min}$ and, thus, a maximum beam widening of the transmission beam. In this scanner system, the number of scan spots in the FoV is equal to the number of microlenses on the microlens array MLA_T, with no subsampling on the detector assumed. Consequently, the pitch of the microlens array MLA_T corresponds to the projected Pitch_{Tr} between the measurement spots in the FoV as well. This again is related to the system angular resolution $\alpha_{Tr} = \tan^{-1}(d_{Tr}/z_{Tr})$, with the transmission spot diameter on the target d_{Tr} at the target distance z_{Tr} [see Fig. 2(b)]. For the following calculations, the Pitch_{MLA_T} of the microlens array MLA_T equates to the diameter of one microlens $d_{\mu L}$. Outgoing from a chosen focal length f_{LO} of the objective lens LO and the resulting horizontal FoV FoV_h, the system-required pitch of the microlens array MLA_T is given as

$$\text{Pitch}_{MLA_T} = \frac{d_{LO} \cdot \tan(\alpha_{Tr})}{2 \cdot \tan\left(\frac{FoV_h}{2}\right)}. \tag{5}$$

This is illustrated in Fig. 3(a) with the example of one standard objective lens LO_1 with a FoV_h of 47 deg and two wide-angle objective lenses LO_2 and LO_3 with 57 deg and 84 deg, respectively. The necessary focal length $f_{\mu L}$ of the microlens with

$$f_{\mu L} = \frac{d_{LO}^2 \cdot \tan(\alpha_{Tr})}{4 \cdot \tan\left(\frac{FoV_h}{2}\right)^2 \cdot d_{T_{LO}}}, \tag{6}$$

to generate a defined transmission beam diameter $d_{T_{LO}}$ on the principle plane of the objective lens LO can be taken from Fig. 3(b). With the specified angular resolution of $\alpha_{Tr} = 0.286$ deg, which is based on a spot diameter in the FoV $d_{Tr} = 0.5$ m at $z_{Tr} = 100$-m target distance, only objective lens LO_1 and LO_2 can meet the requirements. This result is with respect to the minimum reachable f-number of the microlens on the microlens array MLA_T. As shown in Fig. 3(b), with the example of LO_3, the necessary focal length $f_{\mu L}$ (dashed green line) is significantly lower than the theoretically feasible minimum focal length $f_{\mu L,min}$ (dotted green line). The result of Fig. 3(b) shows the limitation of a maximum FoV of the defined system of ± 28.5 deg horizontally with $f_{\mu L} = 99.6$ μm and $\text{Pitch}_{MLA_T} = 99.6$ μm at $d_{T_{LO}} = 20$ mm (red dashed and dotted line one above the other).

Theoretically, our scanner concept realizes transmission beam diameters up to 20 mm over the entire FoV, limited by the clear aperture at the system exit plane on the objective lens LO. Because of the micro-optical-based beam widening, the transmission beam can be deflected with a dimensionally

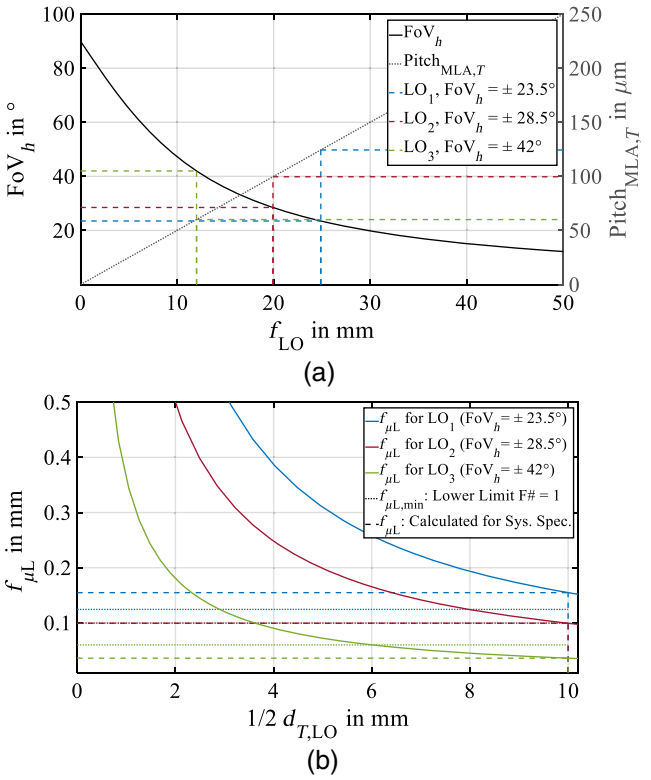

Fig. 3 Geometrical correlation between microlens parameters, horizontal FoV FoV_h, and transmission beam diameter $d_{\mathrm{T_{LO}}}$ with predefined angular resolution $\alpha_{\mathrm{Tr}} = 0.286$ deg (for three objective lenses LO_1, LO_2, and LO_3 with a FoV_h of 47 deg, 57 deg, and 84 deg). (a) The resulting $\mathrm{Pitch}_{\mathrm{MLA_T}}$ to reach the specified resolution with given objective lenses and their focal lengths f_{LO}. (b) The resulting focal length $f_{\mu\mathrm{L}}$ and its lower limit $f_{\mu\mathrm{L,min}}$ of one microlens to realize a specific transmission beam diameter $d_{\mathrm{T_{LO}}}$, exemplarily for $d_{\mathrm{T_{LO}}} = 20$ mm. This is based on the resulting $\mathrm{Pitch}_{\mathrm{MLA_T}}$ from (a), which is given by the defined objective lenses LO_1, LO_2, and LO_3.

small oscillating mirror. In conformity with the IEC 60825-1:2014 standard, our scanner system allows, with an assumed spot diameter of 20 mm, maximum permissible exposures (MPEs) of <4 kW peak power within 2.5-ns full width at half maximum (FWHM) at a wavelength of 900 nm. A high level of transmission power is indispensable for long measurement distances, considering a minimum measurable value of the receiving signal P_{R} in a range of 10^{-9} to 10^{-12} W at the detector. This is based on a huge loss of backscattered signal power even at ideal 100% scattering targets in the FoV with respect to the transmission signal P_{T} (e.g., $P_{\mathrm{R}} \approx P_{\mathrm{T}} \cdot 10^{-8}$ at $z_{\mathrm{Tr}} = 100$ m). We can express the behavior of the receiving signal depending on the ratio of etendues[28] G_{LO} to G_{Tr} of the receiving aperture and that of the backscattered signal at the target ($P_{\mathrm{R}} \propto \frac{G_{\mathrm{LO}}}{G_{\mathrm{Tr}}}$). The MPE power[29,30] $P_{\mathrm{T,max}}$ scales with the beam diameter $d_{\mathrm{T_{LO}}}$ with $P_{\mathrm{T,max}} \propto d_{\mathrm{T_{LO}}}^2$.

For our experimental setup we choose a light-sensitive objective lens LO with a f-number of 1.2 and a FoV_h of ±23.5 deg (necessary $\mathrm{Pitch}_{\mathrm{MLA_T}} = 124.8$ µm) (see Table 1). The microlenses used for the transmission beam widening allow a transmission beam diameter $d_{\mathrm{T_{LO}}}$ of 10.41 mm and consequently a possible transmission pulse-power maximum $P_{\mathrm{T,max}}$ of up to 1 kW, consistent with the IEC 60825-1:2014 standard.

Table 1 System specifications of the experimental setup of the laser scanner module.

Symbol	Value	Description
FoV_h	±23.5 deg	Horizontal FoV
z_{Tr}	0.9 m	Target/object distance
$d_{\mathrm{T_{LO}}}$	10.41 mm	Transmission beam diameter at objective lens LO
P_{T}	<1 kW	Transmission pulse power at 900-nm wavelength
t_{Pulse}	2.5 ns	Transmission pulse length

3 Suppression of Spot Position Noise

In Sec. 3, we show the geometrical correlation between the mirror-deflection noise of the oscillating mirror and the position accuracy of measurement spots in the FoV. We describe how to suppress this position noise in the FoV with the approach of a careful design of the aperture stop dimensions between the microlenses and the transmission beam diameter on the microlens array. Outgoing from the mirror-deflection noise, we show the effect on varying transmission power and spot homogeneity. Further, we give an estimation of the transmission power consumption for a position-noise-suppressed system.

3.1 *Correlation between Mirror-Deflection Angle and Spot Position in the Field of View*

One deflection angle of the oscillating mirror μM correlates with one particular position of the transmission beam on the microlens array $\mathrm{MLA_T}$ in the xy-plane (see Fig. 4). Outgoing from this position, the transmission beam is projected through the objective lens LO into the FoV and directly defines the field angle w_{FoV} and spot position on the target. Consequently, angular mirror-deflection noise of the oscillating mirror leads directly to spot position noise on the microlens array and finally to spot position noise in the FoV. Next to externally induced perturbations, mirror-deflection noise is the dominant limitation for the position accuracy of measurement spots.

On dependence of an arbitrary rotation angle $\varphi_{\mu\mathrm{M}}$, we can express the functional correlation to the corresponding spot

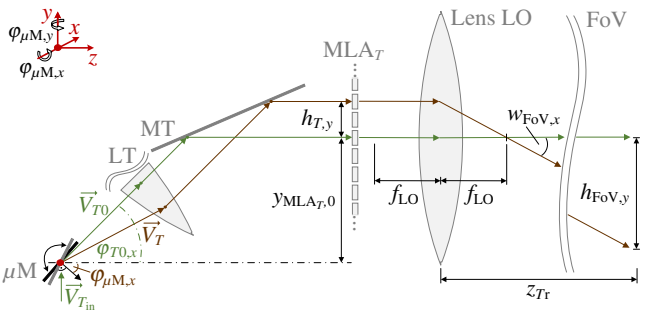

Fig. 4 Scanner section with the geometrical correlation of the resulting spot position on the microlens array and in the FoV in the xy-plane depending on the mirror-deflection angle $\varphi_{\mu\mathrm{M},x}$ of the rotating mirror μM. These positions are given with the radial distance $h_{\mathrm{T},y}$ and $h_{\mathrm{FoV},y}$ from the optical axis of the objective lens LO. For better clarity, just the yz-plane is shown here.

positions in the xy-plane on the microlens array $\mathrm{MLA_T}$ and in the FoV. Through the DCM rotation convention with $\vec{V}_{\mathrm{u,N}} = \mathrm{DCM}_y[\mathrm{DCM}_x \cdot \vec{V}_{\mathrm{u},z}]$, in a first step, we calculate the normalized normal vector of the mirror surface $\vec{V}_{\mathrm{u,N}}$, where $\vec{V}_{\mathrm{u},z}$ is the unit vector in z-direction. With the normalized transmission beam vector

$$\vec{V}_{\mathrm{u,T}} = -\vec{V}_{\mathrm{u,T_{in}}} + 2 \cdot (\vec{V}_{\mathrm{u,N}} \cdot \vec{V}_{\mathrm{u,T_{in}}}) \cdot \vec{V}_{\mathrm{u,N}}, \tag{7}$$

the angle $\varphi_{\mathrm{T,T0}} = \cos^{-1}(\vec{V}_{\mathrm{u,T}} \cdot \vec{V}_{u,\mathrm{T0}})$ in the plane between $\vec{V}_{\mathrm{u,T}}$ and normalized vector $\vec{V}_{\mathrm{T0}}$ on the optical axis of lens LT, the deflected transmission beam vector $\vec{V}_{\mathrm{T}}$ is given as

$$\vec{V}_{\mathrm{T}} = \vec{V}_{\mathrm{u,T}} \cdot \frac{f_{\mathrm{LT}}}{\cos(\varphi_{\mathrm{T,T0}})}. \tag{8}$$

Here, $\vec{V}_{\mathrm{u,T_{in}}}$ describes the known normalized vector of the laser source and f_{LT} denotes the focal length of lens LT. The resulting spot position of the transmission beam in the xy-plane on the microlens array $\mathrm{MLA_T}$ and in the FoV is expressed by its radial distance $\vec{h}_{\mathrm{T}}$ and $\vec{h}_{\mathrm{FoV}}$, with respect to the optical axis of the objective lens LO, as

$$\vec{h}_{\mathrm{T}} = \begin{bmatrix} V_{\mathrm{T},x} \\ -\left(\frac{V_{\mathrm{T0},y} - V_{\mathrm{T},y}}{\cos(\varphi_{\mathrm{T0},x})}\right) \end{bmatrix} \tag{9}$$

and

$$\vec{h}_{\mathrm{FoV}} = -(z_{\mathrm{Tr}} - f_{\mathrm{LO}}) \cdot \begin{pmatrix} \frac{h_{\mathrm{T},x}}{f_{\mathrm{LO}}} \\ \frac{h_{\mathrm{T},y}}{f_{\mathrm{LO}}} \end{pmatrix}. \tag{10}$$

The angle between the lens LT and the optical axis of the system is given as $\varphi_{\mathrm{T0},x}$. The variable z_{Tr} represents the target distance and f_{LO} is the focal length of the objective lens LO. The side inversion because of the reflection on mirror MT and the projection through the lens LO are considered with a negative sign each.

With Eq. (9) we can derive the propagation of the angular error $D\varphi_{\mu\mathrm{M}}$ of the oscillating mirror μM, which is based on the mirror-deflection noise, to the resulting position error Dh_{T} on the microlens array in the xy-plane, as

$$Dh_{\mathrm{T},y} = \left|\frac{\partial h_{\mathrm{T},y}(\varphi_{\mu\mathrm{M},x}, \varphi_{\mu\mathrm{M},y})}{\partial \varphi_{\mu\mathrm{M},x}}\right| \cdot D\varphi_{\mu\mathrm{M},x} + \left|\frac{\partial h_{\mathrm{T},y}(\varphi_{\mu\mathrm{M},x}, \varphi_{\mu\mathrm{M},y})}{\partial \varphi_{\mu\mathrm{M},y}}\right| \cdot D\varphi_{\mu\mathrm{M},y}. \tag{11}$$

Here, exemplarily the y-component is shown (see Fig. 4). We assume an equal probability density distribution of this mirror-deflection noise for calculating the angular uncertainty of the mirror μM with $u_{\varphi_{\mu\mathrm{M}}} = D\varphi_{\mu\mathrm{M},x}/\sqrt{3}$. Accordingly, the combined uncertainty of the transmission beam position on the microlens array $\mathrm{MLA_T}$ for two uncorrelated input parameters is expressed as

$$u_{\mathrm{h_{T},y}} = \sqrt{(C_2)^2 \cdot u^2_{\varphi_{\mu\mathrm{M},x}} + (C_3)^2 \cdot u^2_{\varphi_{\mu\mathrm{M},y}}}, \tag{12}$$

where $C_2 = \frac{\partial h_{\mathrm{T},y}(\varphi_{\mu\mathrm{M},x}, \varphi_{\mu\mathrm{M},y})}{\partial \varphi_{\mu\mathrm{M},x}}$ and $C_3 = \frac{\partial h_{\mathrm{T},y}(\varphi_{\mu\mathrm{M},x}, \varphi_{\mu\mathrm{M},y})}{\partial \varphi_{\mu\mathrm{M},y}}$.

Based on Eq. (10), the position error in the FoV $Dh_{\mathrm{FoV},y}$ and the spot position uncertainty in the FoV $u_{\mathrm{h_{FoV},y}}$ are derived analog to this.

3.2 *Approach for Suppression of Spot Position Noise with Aperture Stops*

In a scanner system with a microlens array in the beam-shaping section with high optical fill factor as shown in Figs. 5(a) and 6(a), the spot position noise on the microlens array $\mathrm{MLA_T}$ is directly projected into the FoV. Here, a position error of the transmission beam $T_{0,Dh_{\mathrm{T}}}$ from the reference position T_0 on the microlens array $\mathrm{MLA_T}$, leads to a position error Dh_{FoV} in the FoV. In our approach, we suppress this direct projection of spot position noise on the microlens array into the FoV with aperture stops between the microlenses and a reduction of the optical fill factor [see Fig. 5(b)].

The diameter of these aperture stops equates to the diameter of the microlenses $d_{\mu\mathrm{L}}$. We design the center-to-center distance of adjacent microlenses $\mathrm{Pitch_{MLA_{T,NS}}}$ to twice the value of the maximum position error $Dh_{\mathrm{T},y}$ of the transmission beam on the microlens array and coat it with light impermeable material

$$\mathrm{Pitch_{MLA_{T,NS}}} = d_{\mathrm{T,MLA_T}} = 2 \cdot \left(\frac{d_{\mu\mathrm{L}}}{2} + Dh_{\mathrm{T},y}\right). \tag{13}$$

Considering this range of the spot position noise, we have to increase the transmission spot diameter $d_{\mathrm{T,MLA_T}}$ on the

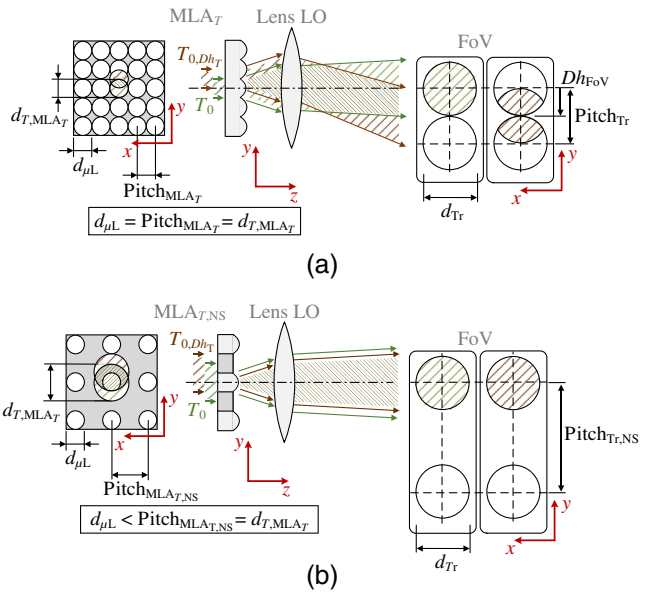

Fig. 5 Schematic principle of the effect of the mirror-deflection noise on the measurement position in the FoV. (a) Transmission path with a microlens array without additional aperture stops; here $\mathrm{MLA_T}$ with $d_{\mu\mathrm{L}} = \mathrm{Pitch_{MLA_T}} = d_{\mathrm{T,MLA_T}}$. (b) Transmission path with a microlens array with additional aperture stops; here, $\mathrm{MLA_{T,NS}}$ with $2 \cdot d_{\mu\mathrm{L}} = \mathrm{Pitch_{MLA_{T,NS}}} = d_{\mathrm{T,MLA_T}}$ for suppression of spot position noise in the FoV.

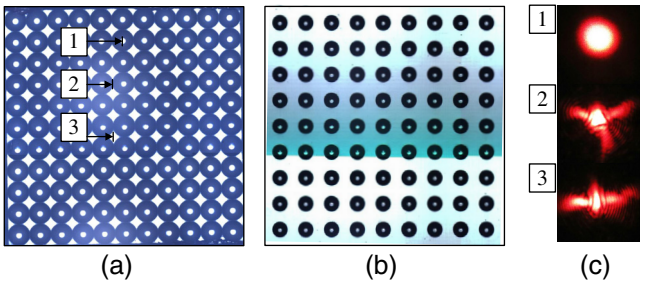

Fig. 6 Microlens arrays utilized in the experiments. (a) MLA_T with $Pitch_{MLA_T} = d_{\mu L}$ (Zeiss SmartZoom m5, 34× Zoom, Plan Apo D 1.6 × /0.1 FWD 36 mm, MLA PowerPhotonics PP-FRF-1464). (b) $MLA_{T,NS}$ with $Pitch_{MLA_{T,NS}} = 2{\cdot}d_{\mu L}$ (Zeiss SmartZoom m5, 34× Zoom, Plan Apo D 1.6 × /0.1 FWD 36 mm, MLA PowerPhotonics PP-FRF-1465). (c) Transmission beam directed on the center of a microlens (1), and on the transition zones between the microlenses (2) and (3), with HRS015B stabilized HeNe laser.

microlens array to the same extent, to ensure fully illuminated microlenses at any time.

Hence, the range of suppression of spot position noise depends on the aperture stop dimension, the pitch between adjacent microlenses and the transmission spot diameter pointing on the microlens array $MLA_{T,NS}$. Our microlens design offers a pitch of twice the diameter of the microlens $Pitch_{MLA_{T,NS}} = 2 \cdot d_{\mu L}$ [see Fig. 6(b)].

With such a microlens array and a focal length $f_{LT} = 75$ mm of lens LT [see Figs. 1(a) and 2(a)], we achieve to suppress a spot position noise in the FoV with a position error of $Dh_{FoV} \approx 0.25$ m ($Dh_t \approx 62.5$ μm on $MLA_{T,NS}$). This means a suppression of mirror-deflection noise with an angular uncertainty of $u_{\varphi_{\mu M,x}} = 0.013$ deg. For small deflection angles, the spot position uncertainty can be assumed as constant. In a system without a position-noise-suppressing microlens array and with an angular resolution $\alpha_{Tr} = 0.286$ deg and a $FoV_h = \pm 23.5$ deg (see Sec. 2.2), this spot position error Dh_{FoV} equates to half the target diameter d_{Tr}, which is to be resolved. This means a spatial degradation of angular resolution up to $\alpha_{Tr_{act}} = ½ \cdot \alpha_{Tr}$. In worst case, targets within the diameter d_{Tr} can be missed, because of emerging gaps between sequential scan spots.

3.3 *Effects of Spot Position Noise on Transmission Power and Spot Homogeneity*

In addition to spot position noise in the FoV, a reduction of the actual transmission power and spot homogeneity is the consequence, if illuminating a microlens not centrically. This reduction depends on the dimension of spot position error of the transmission beam position on the microlens array to the center position of the microlens in the xy-plane. Variations of transmission power and spot homogeneity directly affect the maximum reachable measurement distance and eye safety.

To evaluate the effect of spot position noise on the transmission power, with a static setup we consciously displace the transmission spot on the microlens array to the center position of the microlens in the y-direction. In Figs. 7(a) and 7(b), we experimentally can show this reduction of transmission power. Outgoing from the reference spot T_0 with $h_{T,y} = 0$, we displace the spot up to T_{0,h_T} with $h_{T,y} = ½ \cdot d_{\mu L}$ of the microlens diameter. For a microlens array without a position-noise-suppressing

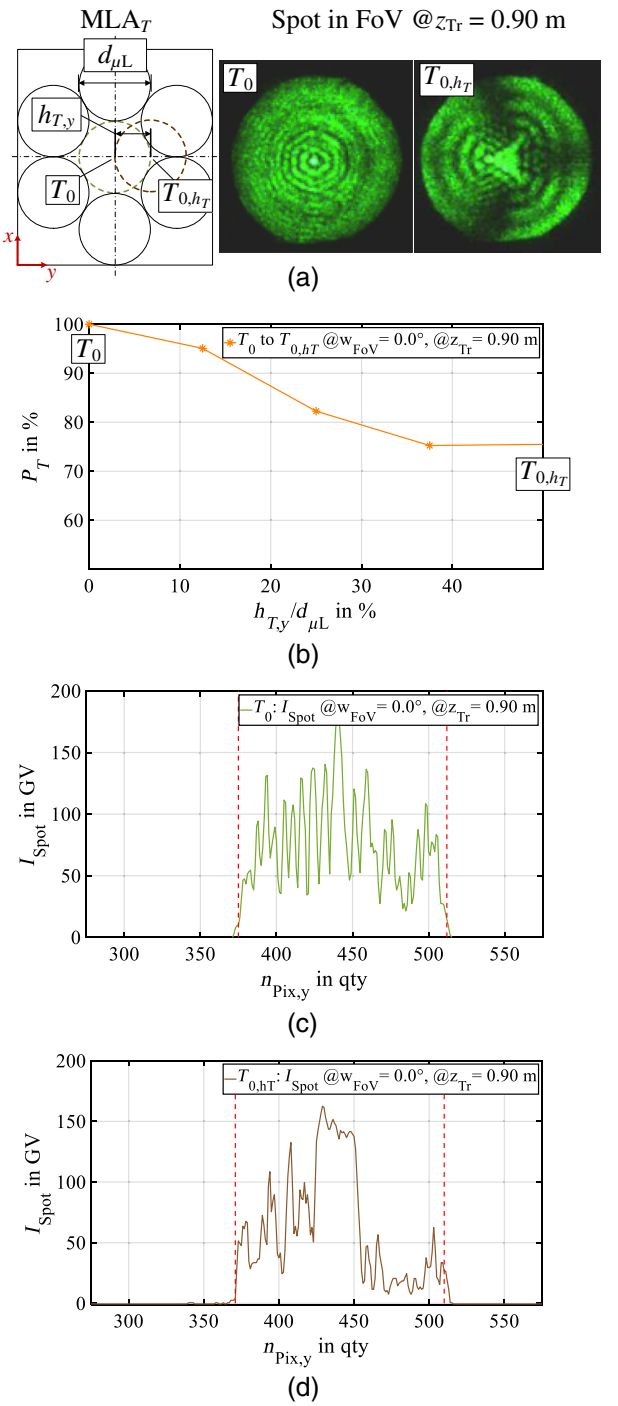

Fig. 7 Transmission power P_T on the target in the FoV, depending on the displacement $h_{T,y}$ (in y-direction) of the transmission beam on the microlens array MLA_T. The illumination is shown for a centric (T_0) position and an eccentric (T_{0,h_T}) position relative to the microlens position. The laser source is a Crylas FDSS 532-Q laser and the transition zones of the microlens array are translucent. (a) The correlation of the transmission spot position on the microlens and its projection into the FoV. (b)The resulting curve of transmission power P_T of the measurement spot in the FoV at $z_{Tr} = 0.90$ m, depending on axial displacement of the transmission beam from the center $h_{T,y} = 0$ to $½ \cdot d_{\mu L}$ of the microlens diameter. (c) Cross section of the transmission spot intensity I_{Spot}, in gray value GV in the FoV at $z_{Tr} = 0.90$ m, T_0: centric illumination of the microlens $h_{T,y} = 0$. (d) Cross section of the transmission spot intensity I_{Spot} in gray value GV in the FoV at $z_{Tr} = 0.90$ m, T_{0,h_T}: eccentric illumination of the microlens $h_{T,y} = ½{\cdot}d_{\mu L}$ (8-bit IDS UI-1450-C USB 2.0 camera).

design [see Figs. 6(a) and 6(c)], eccentric illumination of the microlens means partial illumination of translucent transition zones between the microlenses on the array $\mathrm{MLA_T}$. We can measure a reduction of transmission power P_T of about 25% from centric to eccentric illumination of the microlens.

To express the homogeneity H_I with respect to the spot intensity I_Spot, we use the mean absolute deviation of all intensity values along the spot cross section in the y-direction to the arithmetic mean value $\overline{I}_\mathrm{Spot}$ of the intensity. We just consider values inside the microlens aperture. Related to the measurement, the parameter i defines camera pixels in the range from i_min to i_max with $\pm ½ \cdot d_{\mu\mathrm{L}}$ [see the red dashed lines in Figs. 7(c) and 7(d)]. With normalization of the mean deviation to $\overline{I}_\mathrm{Spot}$, we can write the homogeneity as

$$H_\mathrm{I} = 1 - \left(\frac{1}{N} \sum_{i=i_\mathrm{min}}^{i_\mathrm{max}} |I_{\mathrm{Spot},i} - \overline{I}_\mathrm{Spot}| \right) \cdot \frac{1}{\overline{I}_\mathrm{Spot}}, \tag{14}$$

where N is the number of intensity summands. In Figs. 7(c) and 7(d), we show the corresponding cross section of the transmission spot intensity in the FoV for the reference and the displaced transmission beam T_0 and T_{0,h_T}. A significant decrease of the spot homogeneity from $H_{\mathrm{I}_{\mathrm{T0}}} = 73.7\%$ to $H_{\mathrm{I}_{\mathrm{T0},h\mathrm{T}}} = 51.1\%$ can be observed with an increase in the displacement $h_{\mathrm{T},y}$.

For a microlens array with a position-noise-suppressing design [see Fig. 6(b)], eccentric illumination of the microlens means a direct increase of the illuminated area on the light impermeable aperture stops. This results in a transmission beam that only partially transmits through the microlens array, which is shown simulatively in Fig. 8.

The consequence is a stronger reduction of transmission power P_T in the FoV compared to the microlens design shown in Fig. 6(a). The transmission power P_T in dependence on the displacement $h_{\mathrm{T},y}$ of the illuminated position to the center position of the microlens can be expressed as

$$P_\mathrm{T} = \iint I_\mathrm{Spot}(x,y) \cdot A_{\mu\mathrm{L}}[x,(y - h_{\mathrm{T},y})]\mathrm{d}y\,\mathrm{d}x. \tag{15}$$

Here, $A_{\mu\mathrm{L}}$ is the translucent area of the microlens, which is convoluted with the spot intensity I_Spot. If we assume a Gaussian intensity profile of the transmission beam, we can write the equation as

$$I_\mathrm{Spot}(x,y) = I_{\mathrm{Spot},0} \cdot \frac{1}{2\pi \cdot \sigma^2} \cdot \exp^{-\frac{(x^2+y^2)}{2\cdot\sigma^2}}, \tag{16}$$

where σ is the standard deviation of the beam profile.[31] Figures 9(a) and 9(b) show the spot intensity I_Spot and the transmission power P_T. This is illustrated for two ratios of beam diameter to microlens diameter, A: $d_{\mathrm{T,MLA_T}} = d_{\mu\mathrm{L}}$ and B: $d_{\mathrm{T,MLA_T}} = 2 \cdot d_{\mu\mathrm{L}}$ with identical transmission power $P_{\mathrm{T_A}} = P_{\mathrm{T_B}}$. On this example, we evaluate the behavior of the spot homogeneity and the transmission power depending on the displacement $h_{\mathrm{T},y}$. The spot diameter $d_{\mathrm{T,MLA_T}}$ is defined with $\pm 2\sigma$.

In Table 2, we show the summary of the simulative evaluation based on the graphs given in Fig. 9. With respect to the spot homogeneity H_I and the relative loss of transmission power $P_{\mathrm{T_{Loss}}}$, we can see the advantageous effect of a diameter ratio B. One negative effect of position-noise-suppressing design of the microlens array is a significant increase of the necessary transmission power compared to a microlens design shown in Fig. 6(a). Thus, the light loss at the aperture leads to a necessary increase of transmission power about the factor 2.19 for a design illustrated in Fig. 8(b).

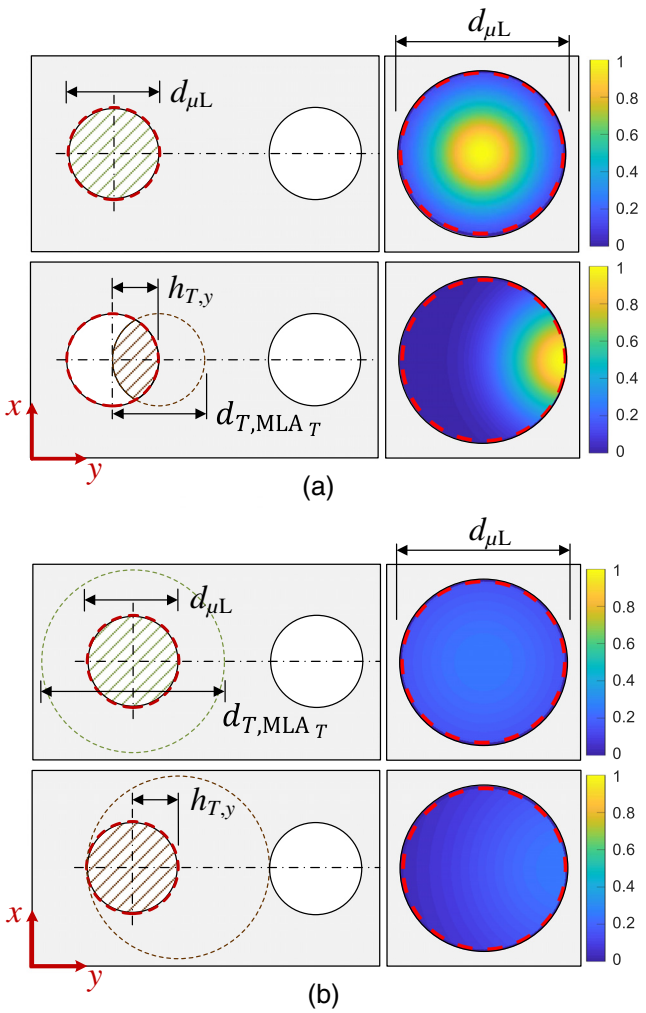

Fig. 8 Transmission spot through the microlens, depending on the displacement $h_{\mathrm{T},y}$ of the transmission beam on the microlens array $\mathrm{MLA_{T,NS}}$. The illumination is shown exemplarily with two ratios (A and B) of beam diameter $d_{\mathrm{T,MLA_T}}$ to microlens diameter $d_{\mu\mathrm{L}}$ on a microlens array with position-noise-suppressing design. This is illustrated for a centric illumination of the microlens with $h_{\mathrm{T},y} = 0$ (upper figure) and an eccentric illumination with $h_{\mathrm{T},y} = ½ \cdot d_{\mu\mathrm{L}}$ (lower figure). The figures on the right of (a) and (b) show the detailed view of one microlens. (a) A: $d_{\mathrm{T,MLA_T}} = d_{\mu\mathrm{L}}$. (b) B: $d_{\mathrm{T,MLA_T}} = 2 \cdot d_{\mu\mathrm{L}}$.

4 Compensation of Spot Shadings

In Sec. 4, we show the drawback of partial shading of measurement spots, while scanning over the FoV. We describe how to avoid this drawback by an optimized optical design of a wedge prism array in the transmission path of the scanner system. Further, we evaluate the effect of spot shadings on the transmission power and consequently on the reachable measurement distance.

4.1 *Principle of Transmission Beam Cutoffs while Scanning over the Field of View*

An inherent characteristic of scanner systems, including micro-optics for beam widening, is the emerging of

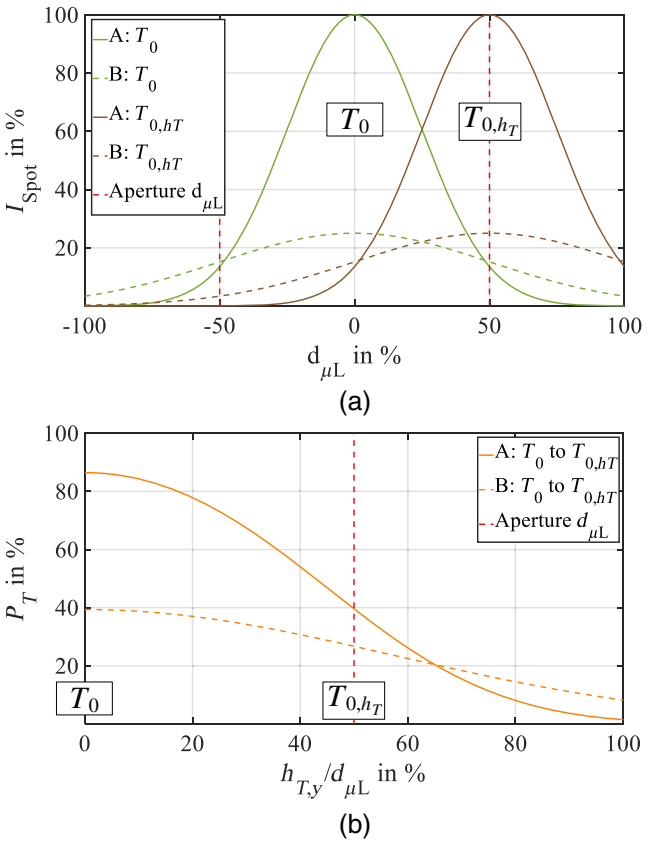

Fig. 9 Effects of spot position noise on transmission power and spot homogeneity. (a) Cross section I_{Spot} in y-direction. (b) Transmission power P_T transmitting through one microlens. With two ratios of beam diameter d_{T,MLA_T} to microlens diameter $d_{\mu L}$,. A: $d_{T,MLA_T} = d_{\mu L}$ and B: $d_{T,MLA_T} = 2 \cdot d_{\mu L}$. This is shown in dependence on the displacement $h_{T,y}$ of the transmission beam from the center $h_{T,y} = 0$ to $h_{T,y} = ½ \cdot d_{\mu L}$ relative to one microlens, described with T_0 and T_{0,h_T}.

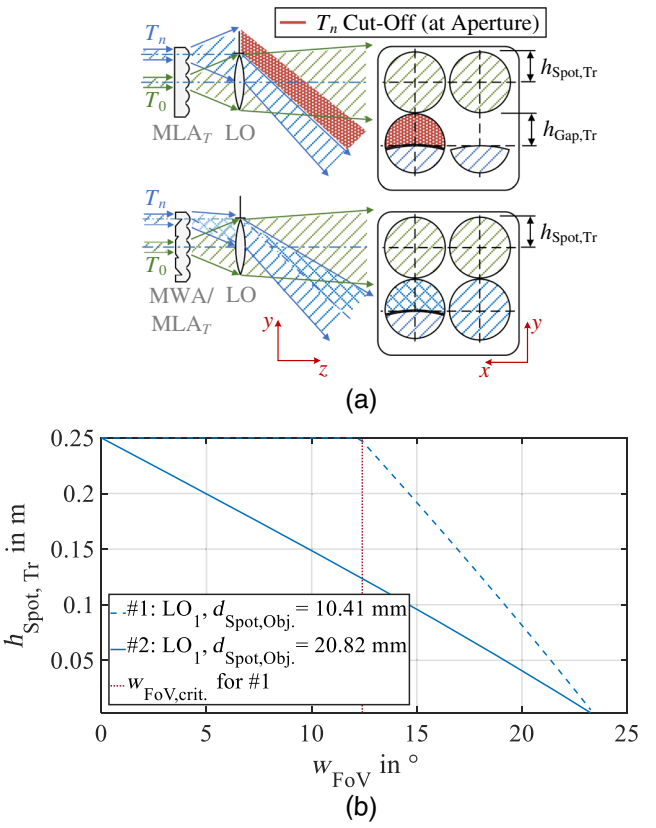

Fig. 10 Influence of transmission beam cutoff on the residual spot height $h_{Spot,Tr}$ and the emerging gap height $h_{Gap,Tr}$ between adjacent spots on the target. (a) Schematic functional principle of the beam-shaping section with and without MLA$_T$/MWA combination. (b) Graph of the residual spot height in the FoV for an objective lens LO$_1$ with a FoV$_h$ of ±23.5 deg without a MLA$_T$/MWA combination at 100-m target distance. This is shown for two spot diameters $d_{T_{LO}}$ = 10.41 mm and $d_{T_{LO}} = d_{LO}$ = 20.82 mm in the plane of the objective lens, where d_{LO} is the diameter of the objective lens.

transmission beam cutoffs at the aperture stop of the objective lens while scanning over the microlens array. The consequences are not only gaps between adjacent spots in the FoV. This also leads to a significant reduction of transmission power with coupled degradation of reachable measurement distance. Beam cutoffs at the aperture stop of the objective lens start at a system-specific incidence height of the transmission beam on the objective lens. This incidence height is transformed into a field angle, which we call the critical field angle $w_{FoV_{crit.}}$. Based on these cutoffs, shadings or gaps $h_{Gap,Tr}$ arise between adjacent measurement spots in the FoV and increase proportional to the tangent of the field angle w_{FoV} [$h_{Gap,Tr} \propto \tan(w_{FoV})$]. The consequence is possible nondetection of targets with higher spatial frequency and the reduction of measurement distance within higher field angles of the scanner system.

By realizing a maximum eye-safe transmission beam with a diameter equal to that of the objective lens LO, the cutoff already starts by the illumination of the first microlens aside the one to the optical axis. At the maximum field angle, the cutoff equates inherently always to half the spot diameter $d_{T_{LO}}$, which inevitably leads to a spot shading in the FoV of half the target diameter d_{Tr}. In Fig. 10(a), this is illustrated with the help of two exemplary transmission beams T_0 and T_n.

Figure 10(b) shows the correlation between the increase of field angle w_{FoV} and the reduction of the residual spot height $h_{Spot,Tr}$ up to 0.25- at 100-m target distance. On the basis of an objective lens with a FoV$_h$ = ±23.5 deg and a diameter d_{LO} = 20.82 mm, we explain this characteristics for two spot diameters $d_{T_{LO}}$ = 10.41 mm and $d_{T_{LO}} = d_{LO}$ =

Table 2 Evaluation of the spot homogeneity H_I and the loss of transmission power $P_{T_{Loss}}$. Here, these values are given in dependence on the transmission spot diameter d_{T,MLA_T} (A and B) on the microlens array MLA$_{T,NS}$ and its displacement $h_{T,y}$ regarding the microlens center position.

Transmission spot diameter on MLA$_T$	$H_{I_{T0}}$ in %	$H_{I_{T0,hT}}$ in %	P_{T_0} in %	$P_{T_{0,hT}}$ in %	rel. $P_{T_{Loss}}$ ($T_0 - T_{0,h_T}$) in %
A: $d_{T,MLA_T} = d_{\mu L}$	56.5	2.1	86.5	40.2	53.5
B: $d_{T,MLA_T} = 2 \cdot d_{\mu L}$	87.2	57.0	39.3	26.9	31.6

20.82 mm in the plane of the objective lens. As we can see, in contrast to a fully illuminated objective lens, a spot diameter of 10.41 mm results in a critical field angle of 12.14 deg, which allows a gapless illuminated FoV of 56.26%. Hence, the percentage of the FoV, which is possible to be scanned without provoking shadings caused by these cutoffs, depends on the optical design of the beam-shaping section and the specified transmission spot diameter.

4.2 *Approach for Compensation of Spot-Shadings with Wedge Prisms*

To avoid this substantial drawback, our optics solution includes a microwedge prism array MWA in addition to the microlens array $\mathrm{MLA_T}$. The microwedge prism array consists of one with the microlens array combined module or of two separate optical components optionally. In Figs. 10(a) and 11(a), the combined and the separate versions are illustrated. We design each wedge prism for one corresponding microlens exclusively. The wedge angle $\gamma_{\mathrm{w},n}$ and the offset $d_{\mathrm{w},n}$ to the optical axis of the corresponding microlens depend on the radial distance $h_{\mu\mathrm{L}}$ to the optical axis of the objective lens LO [see Fig. 11(c)]. The microwedge prism

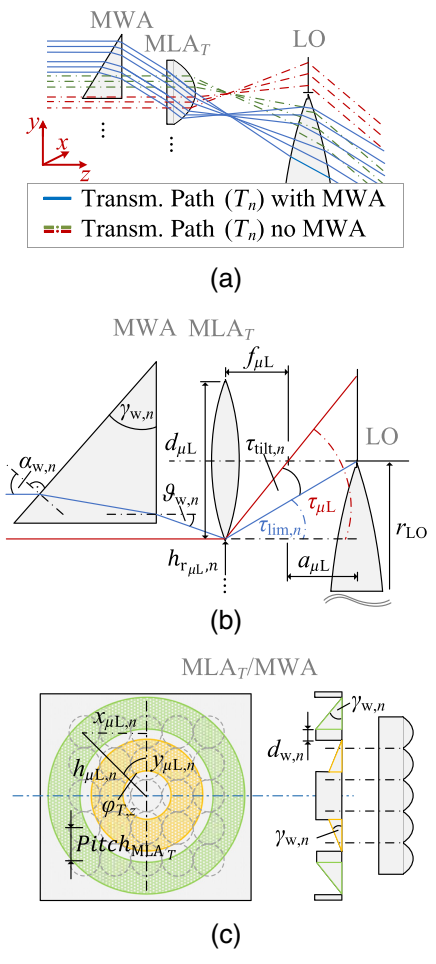

Fig. 11 Detailed functional principle of the microlens array/microwedge prism array $\mathrm{MLA_T}$/MWA combination. (a) Comparison of the optical transmission path between using a $\mathrm{MLA_T}$/MWA component and a single $\mathrm{MLA_T}$ component without MWA. (b) Geometrical correlation of the necessary tilt angle $\tau_{\mathrm{tilt},n}$ and the resulting wedge angle $\gamma_{\mathrm{w},n}$ of the wedge prism. (c) Schematic design of a $\mathrm{MLA_T}$/MWA component.

array refracts the divergent light cone of the transmission signal after the microlens for each scan position by exactly the amount that it can pass the objective lens LO without any cutoff at the aperture stop. We show in Fig. 11(b) the geometrical fundamentals for the calculation of the necessary tilt angle $\tau_{\mathrm{tilt},n}$ and the resulting wedge angle $\gamma_{\mathrm{w},n}$.

From Fig. 11(c), we can calculate the radial distance of the aperture of each microlens $h_{\mathrm{r}_{\mu\mathrm{L}},n}$ to the optical axis of the objective lens LO with $y_{\mu\mathrm{L},n} = n_{\mu\mathrm{L},y} \cdot \mathrm{Pitch_{MLA_T,y}}$, $x_{\mu\mathrm{L},n} = n_{\mu\mathrm{L},x} \cdot \mathrm{Pitch_{MLA_T,x}}$, and $h_{\mu\mathrm{L},n} = \sqrt{x_{\mu\mathrm{L},n}^2 + y_{\mu\mathrm{L},n}^2}$, which can be expressed as

$$h_{\mathrm{r}_{\mu\mathrm{L}},n} = h_{\mu\mathrm{L},n} - r_{\mu\mathrm{L}}. \tag{17}$$

Here, $n_{\mu\mathrm{L},x}$ and $n_{\mu\mathrm{L},y}$ is the number of the particular microlens (in x- and y-directions), starting the numeration with the element on the optical axis of the objective lens LO.

The radial distance of the center of each particular microlens to this optical axis is given with $h_{\mu\mathrm{L},n}$ and the radius of the microlens with $r_{\mu\mathrm{L}} = ½ \cdot d_{\mu\mathrm{L}}$. The necessary tilt angle $\tau_{\mathrm{tilt},n}$ of the marginal ray of each microlens is expressed as

$$\tau_{\mathrm{tilt},n} = \tau_{\mu\mathrm{L}} - \tau_{\mathrm{lim},n} = \tan^{-1}\left(\frac{\frac{r_{\mu\mathrm{L}}}{f_{\mu\mathrm{L}}} - \frac{r_{\mathrm{LO}} - h_{\mathrm{r}_{\mu\mathrm{L}},n}}{a_{\mu\mathrm{L}} + f_{\mu\mathrm{L}}}}{1 + \frac{r_{\mu\mathrm{L}}}{f_{\mu\mathrm{L}}} \cdot \frac{r_{\mathrm{LO}} - h_{\mathrm{r}_{\mu\mathrm{L}},n}}{a_{\mu\mathrm{L}} + f_{\mu\mathrm{L}}}}\right), \tag{18}$$

with $\tau_{\mu\mathrm{L}}$ the maximum divergence angle of the light cone, assuming an entirely illuminated microlens. The tilt angle $\tau_{\mathrm{lim},n}$ describes the maximal angle, which can pass the objective lens LO with $d_{\mathrm{LO}} = 2 \cdot r_{\mathrm{LO}}$. We can equate $\tau_{\mathrm{tilt},n}$ with the deflection angle of the wedge prism $\vartheta_{\mathrm{w},n}$. With the assumption of $\gamma_{\mathrm{w},n} \Rightarrow \alpha_{\mathrm{w},n} = \gamma_{\mathrm{w},n}$ between the incidence angle $\alpha_{\mathrm{w},n}$ of the transmission signal at the wedge prism and the wedge angle $\gamma_{\mathrm{w},n}$, we can write the equation as

$$\gamma_{\mathrm{w},n} = \sin^{-1}\sqrt{\left(\frac{(1+n_{\mathrm{w}}^2)\cdot\sin(\vartheta_{\mathrm{w},n}) \pm 2\cdot\sin(\vartheta_{\mathrm{w},n})^2\, C_4}{4\cdot\sin(\vartheta_{\mathrm{w},n})^2 + (1+n_{\mathrm{w}}^2)^2}\right)}, \tag{19}$$

where $C_4 = \sqrt{n_{\mathrm{w}}^2 - \sin(\vartheta_{w,n})^2}$.

The refraction index of the wedge prism material is given with n_{w}.

4.3 *Effects of Beam Cutoffs on Transmission Power and Residual Spot Height*

We experimentally investigate the optimized micro-optical component, to demonstrate the improvement of a $\mathrm{MLA_T}$/MWA combination in a scanner system and to prove the theoretical calculations. The scanner setup provides a FoV of ±23.5 deg, a beam diameter of $d_{\mathrm{T_{LO}}} = 10.41$ mm, and a measurement distance of 0.90 m. Our tests reveal a high consistency between theoretical simulation and measurement [see Fig. 12(a)]. We can show that a setup with a microwedge prism array in the optical path increases the transmission signal in the FoV by the factor of 2.47 compared to that without such a component. In consequence, this theoretically leads to a rise of measurement distance ($\sqrt{P_{\mathrm{T}}} \propto z_{\mathrm{Tr}}$)[26] of about the factor of 1.57, assuming a fully illuminated target with a minimum diameter d_{Tr}.

The drop of the curve with $\mathrm{MLA_T}$/MWA combination is based on the incidence angle $\vartheta_{\mathrm{w},n}$ into the microlens, which

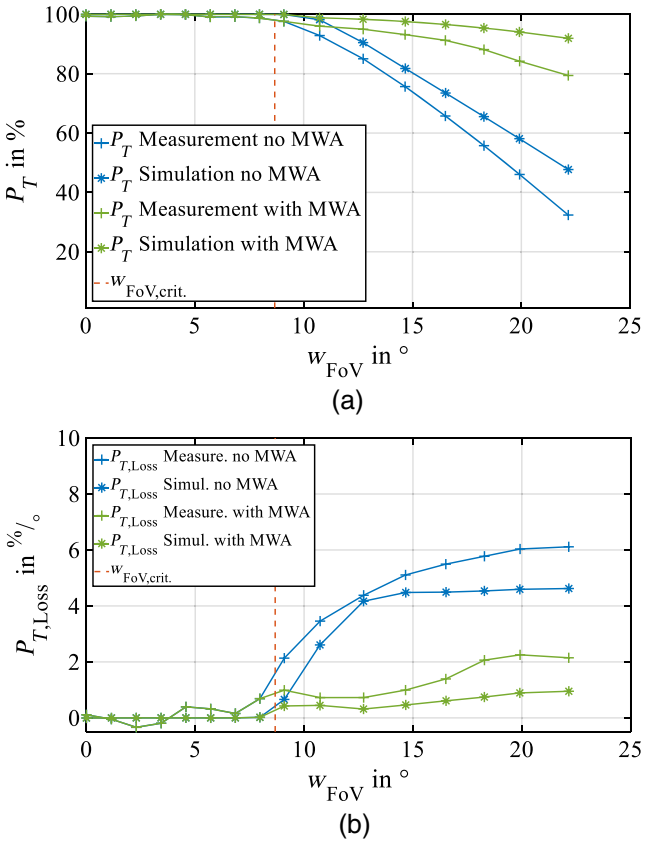

Fig. 12 Measurement of transmission power P_T over the field angle w_{FoV} for an objective lens LO_1 with a FoV_h of ±23.5 deg. (a) P_T over w_{FoV} in comparison between simulation and measurement values. (b) Gradient of the loss of transmission power $P_{T_{Loss}}$ over w_{FoV}. The red dashed line gives the critical angle $w_{FoV_{crit.}}$, where the beam cutoff starts theoretically.

increases the spot diameter with a cosine function in this plane. The result is less effective signal transmitting through the microlens. However, this can be avoided by rotating the microlens with the equal value to the value of $\vartheta_{w,n}$ or inverting the sequence of the components itself, which again leads to higher effort in appropriate lens design.

The gradient of the transmission power loss $P_{T_{Loss}}$ in the FoV is given in Fig. 12(b). The curve shows the characteristic for an axial displacement in y-direction [similar to Fig. 10(a)] of a rectangular light cone to an objective lens with a round aperture stop. Because of the experimentally used rectangular microlens aperture, the critical field angle $w_{FoV_{crit.}} = 8.67$ deg (red dashed line) is lower than the calculated angle of LO_1 with a round microlens aperture, which is shown in Fig. 10(b). In the experiment, we see that the reduction of transmission power P_T of the measured curve is higher compared to the simulated curve. The reason for this is the telecentric characteristics of the objective lens LO utilized in the experiments. In such a lens, the clear aperture decreases significantly with higher scan angles w_{FoV}. This also causes the increasing deviation between simulation and measurement curves with increasing w_{FoV}. We can avoid this issue with appropriate lens design of the objective lens LO as well.

In Fig. 13, we try to clarify the effects of transmission beam cutoff at the aperture stop of the objective lens LO on the residual spot height $h_{Spot,Tr}$, which is projected on the target at 0.45-m target distance. In the first row, we see the decrease of $h_{Spot,Tr}$ for defined field angles $w_{FoV} =$ 0.00 deg, 9.09 deg, 16.51 deg, and 22.16 deg without MLA_T/MWA combination. Starting at the critical field angle $w_{FoV_{crit}}$, the value of $h_{Spot,Tr}$ shows the behavior of $h_{Spot,Tr} \propto -\tan(w_{FoV})$. In the second row with the MLA_T/MWA combination, the upper cutoff of the corners arises from rounding errors between the calculated radial distance to the optical axis and the utilized wedge prism with given wedge angle $\gamma_{w,n}$. The lower cutoff starting at 16.51 deg and increasing significantly at 22.16 deg is based on the

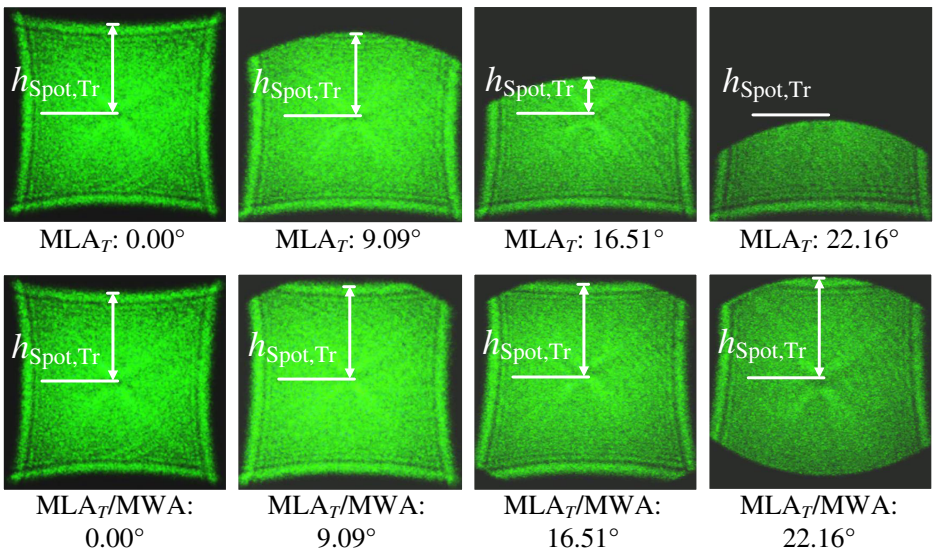

Fig. 13 Effect of transmission beam cutoff on the spot geometry and the residual spot height $h_{Spot,Tr}$ on the target. Here, the figures show the comparison between the spots for several field angles w_{FoV} at 0.45-m target distance with and without a microlens array/microwedge prism array combination (MLA_T/MWA).

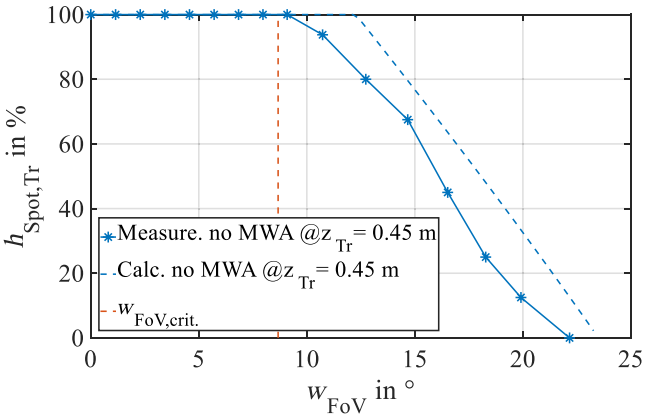

Fig. 14 Measurement of spot height $h_{Spot,Tr}$ over the field angle w_{FoV} for an objective lens LO_1 with a FoV_h of ±23.5 deg without a MLA_T/MWA combination. The red dashed line gives the critical angle $w_{FoV_{crit.}}$, where the beam cutoff starts theoretically.

already-mentioned telecentric characteristics of the utilized objective lens LO.

In Fig. 14, we show the measurement of the decreasing residual spot height, while scanning up to a field angle of 22.16 deg without a microwedge prism component. Here, the measurement result shows good consistency to simulated values. The reduction of the spot height starts at a smaller field angle with 10.73 deg compared to that of the simulation with 12.14 deg. This is based on a minimal smaller diameter of the aperture stop of the objective lens used in the experiments as assumed in the simulation.

5 Conclusion

For an eye-safe scanner system, we show principal limitations regarding the angular resolution and the maximum possible diameter of the transmission beam. The upper limit for the transmission beam diameter is about 20 mm with a diameter of microlenses of 99.6 μm. This is calculated for a micro-optics-based scanner system with an angular resolution of 0.286 deg. Such an angular resolution equates to the resolution of a target with the diameter 0.5-m at 100-m target distance, assuming an f-number of the microlens of ≥1. The system allows MPEs of ≥4 kW peak power within 2.5 ns FWHM at 900-nm wavelength. Here, a FoV of ±28.5 deg is reachable with a diameter of the objective lens of 20.82 mm.

To suppress spot position noise in the FoV, we present an approach of an optimized microlens array with carefully designed aperture stops in the transmission path. We are able to suppress a mirror-deflection noise with an angular uncertainty of 0.013 deg. This equates to a suppression of a spot position error of about 0.25-m at 100-m target distance. With our approach, we additionally improve the transmission power loss by about 21.6% and the transmission spot homogeneity by about 54.9%, depending on the level of spot position error on the microlens array. The power consumption of a setup with position-noise-suppressing microlens design is about a factor 2.19 higher compared to a setup without this design.

The scanner system, presented in this paper, allows a small rotating mirror and provides a high spot position accuracy of measurement spots in the FoV without any shadings in between. With the combination of a microlens array and a microwedge prism array in the optical transmission path, we can show a nearly perfect compensation of transmission beam cutoffs at the aperture stop of the objective lens. In consequence, we avoid the resulting shadings between adjacent spots in the FoV up to half the specified target diameter, which is to be resolved. This realizes not only a gapless illuminated FoV but also a significant increase of transmission signal by a factor of 2.47. Theoretically, this leads to a rise of measurement distance of about a factor of 1.57, derived from the radiometric inverse square law.[26]

Our experimental setup offers an objective lens with 20.82 mm diameter and a FoV of ±23.5 deg at 0.90-m target distance. The FoV can be scanned with a deflection angle of the oscillating mirror of about ±3.95 deg at 75-mm focal length of the lens LT. We utilize a microlens with an f-number of 2.4, which generates a spot diameter of 10.41 mm at the system exit plane on the objective lens. The MPE of this setup is about 1 kW transmission peak power.

Acknowledgments

The presented work has been developed in collaboration with Robert Bosch GmbH and the Clausthal University of Technology. The authors sincerely acknowledge the support and want to thank all contributors and colleagues for their helpful inputs and discussions to realize this project.

References

1. "High definition LiDAR system," U.S. Patent No. 008,767,190 B2, Velodyne Acoustics Inc. (2014).
2. G. Pennecot et al., "Devices and methods for a rotating LIDAR platform with a shared transmit/receive path," U.S. Patent No. 8,836,922, p. B1, Google Inc. (2014).
3. M. Beer et al., "1 × 80 pixel SPAD-based flash LIDAR sensor with background rejection based on photon coincidence," in *IEEE SENSORS*, pp. 1–3 (2017).
4. ASC, Advanced Scientific Concepts, "Peregrine 3D flash LIDAR vision system," http://www.advancedscientificconcepts.com/products/peregrine.html (27 January 2019).
5. H. Kaartinen et al., "Benchmarking the performance of mobile laser scanning systems using a permanent test field," *MDPI Sens.* **12**(9), 12814–12835 (2012).
6. B. Davis, "Innovative technology workshop on 3D LiDAR," Research Project Final Report, Center for Transportation Studies, University of Minnesota (2016).
7. RIEGL Laser Measurement Systems GmbH, "RIEGL VMQ-1H," http://www.rieglusa.com/pdf/vmq-1ha-datasheet1.pdf (29 January 2019).
8. A. Süss et al., "Benchmarking time-of-flight based depth measurement techniques," *Proc. SPIE* **9751**, 975118 (2016).
9. T. Sander et al., "Large aperture MEMS scanner module for 3D distance measurement," *Proc. SPIE* **7594**, 75940D (2010).
10. U. Hofmann et al., "Resonant biaxial 7 mm-MEMS mirror for omnidirectional scanning," *J. Micro/Nanolithogr. MEMS MOEMS* **13**(1), 011103 (2013).
11. A. Day et al., "Lidar systems and methods for detection and classification of objects," WO 2018/127789, p. Al, Innoviz Technologies Ltd. (2018).
12. K. Ito et al., "System design and performance characterization of a MEMS-based laser scanning time-of-flight sensor based on a 256 × 64-pixel single-photon imager," *IEEE Photonics J.* **5**(2), 6800114 (2013).
13. S. T. S. Holmström, U. Baran, and H. Urey, "MEMS laser scanners: a review," *J. Microelectromech. Syst.* **23**(2), 259–275 (2014).
14. X. Cheng et al., "An integrated optoelectronic position sensor for MEMS scanning mirrors," in *IEEE 19th Int. Conf. Solid-State Sens., Actuators and Microsyst. (TRANSDUCERS)*, pp. 2179–2182 (2017).
15. T. Sandner et al., "Integrated piezoresistive positionsensor for micro-scanning mirrors," in *IEEE/LEOS Int. Conf. Opt. MEMS and Nanophotonics*, pp. 195–196 (2007).
16. T. K. Chan et al., "Optical beamsteering using an 8 × 8 MEMS phased array with closed-loop interferometric phase control," *Opt. Express* **21**(3), 2807–2815 (2013).
17. B. Cagdaser et al., "Capacitive sense feedback control for MEMS beam steering mirrors," in *Proc. Solid-State Sens., Actuator and Microsyst. Workshop*, Hilton Head Island, South Carolina, pp. 6–10 (2004).

18. P. Brosens, "Dynamic mirror distortions in optical scanning," *Appl. Opt.* **11**(12), 2987–2989 (1972).
19. H. Urey, D. W. Wine, and J. R. Lewis, "Scanner design and resolution trade-offs for miniature scanning displays," *Proc. SPIE* **3636**, 60–68 (1999).
20. H. Schenk et al., "Design and modeling of large deflection micromechanical 1D and 2D scanning mirrors," *Proc. SPIE* **4178**, 116–125 (2000).
21. T. Klose, "Modellierung und Entwurf von resonanten Mikroaktoren mit elektrostatischem Antrieb," Fakultät Elektrotechnik und Informationstechnik, Technische Universität Dresden (2016).
22. J. Hasselbach, "Laser scanner, for example, for a lidar system of a driver assistance system," WO2018/197246, p. AI, Robert Bosch GmbH (2018).
23. J. Hasselbach, S. Bogatscher, and C. Rembe, "Laser scanning module with large sending aperture and inherent high angular position accuracy for 3D LiDAR," *Proc. SPIE* **11028**, 1102804 (2019).
24. H.-J. Schwarz et al., "Lidar sensor," DE 10 2015 217 908, p. A1, Robert Bosch GmbH (2017).
25. H. D. Tholl et al., "Modul für ein Lasermessgerät mit Glasfaser und bidirektionaler optischer Verstärkung," EP 1 589 353, p. A1, Diehl BGT Defence GmbH & Co. KG (2005).
26. A. Pacala et al., "Optical system for collecting distance information within a field," U.S. Patent No. 20,180,217,236 A1, Ouster Inc. (2018).
27. F. Pedrotti et al., *Optik für Ingenieure*, 3rd edn., pp. 13, 14, 65, Springer-Verlag, Berlin, Heidelberg, New York (2005).
28. O. Reeb, *Grundlagen der Photometrie*, pp. 12–18, G. Braun, Karlsruhe (1962).
29. R. Henderson and K. Schulmeister, *Laser Safety*, 1st edn., pp. 88, 135, 136, 156, Taylor and Francis Group, LLC, New York (2004)
30. IEC 60825-1:2014, *Sicherheit von Lasereinrichtungen*, pp. 35, 40, 44, VDE Verlag GmbH, Berlin (2014)
31. J. Eichler, L. Dünkel, and B. Eppich, "Die Strahlqualitaet von Lasern-Wie bestimmt man Beugungsmasszahl und Strahldurchmesser in der Praxis?" *Laser Tech. J.* **1**(2), 63–66 (2004).

Jürgen Hasselbach received his diploma degree in mechatronics and microsystems from Heilbronn University of Applied Sciences, Germany, in 2010. From 2010 to 2016, he worked at the Robert Bosch GmbH as development engineer in optical testing for video-based automotive driver assistance systems. Since 2016, he has been a PhD student at Clausthal University of Technology in cooperation with the Robert Bosch GmbH. The subject of his work is the development and investigation of a LiDAR scanner module with large sending/receiving apertures and high angular position accuracy.

Siegwart Bogatscher received his diploma in electrical engineering from the University of Karlsruhe (TH), Germany, in 2009. He was a PhD student at the Karlsruhe Institute of Technology (KIT) from 2009 to 2014 and received his doctorate degree in electrical engineering. In 2015, he joined Robert Bosch GmbH. As a system architect, he works in the field of LiDAR development for autonomous driving applications.

Christian Rembe received his diploma in physics from the University of Hanover, Germany, in 1994. From 1994 to 1999, he was a PhD student at the University of Ulm, Germany, where he earned a doctorate degree in electrical engineering. In 1999, he joined the Berkeley Sensor & Actuator Center at the University of California, Berkeley, as a postdoctoral research engineer with the support of a Feodor-Lynen-Scholarship of the Alexander von Humboldt-Foundation and a UC Berkeley MacKay-Lecturer Fellowship. From 2001 to 2014, he was the manager of the Development Optics group at the Polytec GmbH in Waldbronn, Germany. Since 2015, he has been a professor for applied metrology at the Clausthal University of Technology, Germany. His interests are optics, optical measurement techniques, sensors, and microelectromechanical systems.